

# Investigation of HgCdTe avalanche photodiodes for HOT condition

Tetiana MANYK<sup>1</sup> , Jan SOBIESKI<sup>1,2</sup>, Kacper MATUSZELAŃSKI<sup>2</sup>, Jarosław RUTKOWSKI<sup>1</sup>, and Piotr MARTYNIUK<sup>1</sup>

<sup>1</sup> Institute of Applied Physics, Military University of Technology, ul. Kaliskiego 2, 00-908 Warsaw, Poland

<sup>2</sup> Vigo Photonics S.A., ul. Poznańska 129/133, 05-850 Ożarów Mazowiecki, Poland

**Abstract.** The performance of long-wave infrared (LWIR)  $x = 0.22$  HgCdTe avalanche photodiodes (APDs) was presented. The dark current-voltage characteristics at temperatures 200 K, 230 K, and 300 K were measured and numerically simulated. Theoretical modeling was performed by the numerical Apsys platform (Crosslight). The effects of the tunneling currents and impact ionization in HgCdTe APDs were calculated. Dark currents exhibit peculiar features which were observed experimentally. The proper agreement between the theoretical and experimental characteristics allowed the determination that the material parameters of the absorber were reached. The effect of the multiplication layer profile on the detector characteristics was observed but was found to be insignificant.

**Keywords:** HgCdTe; APD; LWIR; MWIR.

## 1. INTRODUCTION

Mercury cadmium telluride (HgCdTe) is an industry-standard material for infrared (IR) detector fabrication and has been widely used for sensitive devices operating within important IR range from 1.3  $\mu\text{m}$  to 16  $\mu\text{m}$  [1–6]. Design and processing of HgCdTe high-performance long-wave infrared (LWIR) avalanche photodiodes (APDs) operating at high temperatures are highly desired for weak signal detections, especially for applications requiring specific device size and power consumption [7]. LWIR detectors are favorable due to imaging applications with high gain and low noise and are widely used in optical communication systems and laser radar detectors [8]. The most extensive work on HgCdTe APD has been carried out by CEA-LETI [9] and the Shanghai Institute of Technical Physics - SITP [10, 11]. They focus on photon-starved and high-speed applications, such as active imaging and free space optical communications.

The main advantage of HgCdTe is the possibility to control the bandgap energy by changing the Cd stoichiometric composition, high electron mobility, and flexibility in controlling the carrier concentration level. Mercury cadmium telluride is a semiconductor material well-suited for APD applications. The IR APDs should exhibit high photocurrent, high gain, and low noise. The electron multiplication in LWIR APDs occurs more easily than in medium-wavelength infrared (MWIR) and short-wavelength infrared (SWIR) diodes [12]. The current numerical theories on avalanche photodetectors mainly fall into two categories: macroscopic empirical model with parameter fitting and micro-

scopic simulation with statistical estimates. Various theoretical approaches were used to describe the avalanche mechanism providing only a qualitative or semi-quantitative explanation of the gain and noise in HgCdTe APDs [13]. Recently, a parameter-free analytical avalanche theory for the low bandgap HgCdTe derived from quantum mechanics was presented to avoid any fitting parameters or statistical estimates used by both theoretical approaches [14]. In this work, we will use the method where impact ionization is defined through the expression for generation (G) rate. Since impact ionization occurs only in high-field regions where the drift terms dominate, Selberherr [15] suggested the use of the equation:

$$G = \frac{\alpha_e J_e}{q} + \frac{\alpha_h J_h}{q}, \quad (1)$$

where  $\alpha_e$  and  $\alpha_h$  are the electron and hole ionization rates,  $q$  is the elementary charge, and  $J_e$  and  $J_h$  are the current densities. Expression for  $\alpha_e$  was first proposed by Chynoweth [16]:

$$\alpha_e = a_e e^{-\frac{b_e}{F}}, \quad (2)$$

where  $b_e$  is the critical field in the multiplication region and coefficient  $a_e$  stands for the inverses of the mean free path between impacts when electric field  $F = \infty$ . A similar expression can be written for the holes.

Generally, the tested Chynoweth ionization model is characterized by the electrons [ $a_e$ ,  $b_e$ ] and holes [ $a_h$ ,  $b_h$ ] parameters. The unequal ionization coefficients of electrons ( $a_e$ ) and holes ( $a_h$ ) originate from the asymmetry between the effective masses of electrons in the conduction band and heavy holes in the valence band. The impact ionization coefficient ( $k = a_h/a_e$ ) determines the semiconductor material's ability for avalanche effect. Coefficient  $k$  is dependent on the molar Cd composition

\*e-mail: [tetjana.manyk@wat.edu.pl](mailto:tetjana.manyk@wat.edu.pl)

Manuscript submitted 2023-09-18, revised 2023-12-22, initially accepted for publication 2024-01-17, published in May 2024.

in HgCdTe [5, 17, 18]. According to Singh *et al.*, electron ionization is advantageous for the LWIR detectors ( $x < 0.5$ ) [19]. The HgCdTe detectors typically operate at the reverse bias lower than 1 V. For the avalanche process, much higher reverse voltages are needed. The multiplication region of APD is important to reach avalanche gain with low multiplication noise and high bandwidth.

Direct tunneling between valence and conduction bands (band-to-band tunneling) in HgCdTe APDs structure under reverse bias by the Zener model was simulated. When a strong external electric field is applied, tunneling of electrons between the conduction and valence band can take place generating electron-hole pairs. Newly created carriers will drift in a strong electric field and can result in impact ionization. Thus, both impact ionization and Zener tunneling electron-hole generation rates should be included in the drift-diffusion model.

Dark current and gain are a set of key indicators that always need trade-offs in practical APDs. The paper presents the study of the LWIR HgCdTe APDs. The influence of absorber layer doping, the effect of tunneling, and the effect of impact ionization on the current-voltage characteristics were analyzed. The theoretical simulation results were compared with the APD designed for HOT conditions.

## 2. EXPERIMENTAL RESULTS

The bottom-side illuminated LWIR HgCdTe heterostructure offers an attractive approach with an APD detector. APD structure is flexible in terms of material growth with reduced defects exhibiting higher gain uniformity and operability [20–24]. The literature analysis shows that the introduction of the barrier limits the dark current compared with APD without a proper barrier layer [25]. The HgCdTe APD structure with the corresponding energy bandgap diagram is shown in Fig. 1 where  $E_c$  is the bottom edge of the conduction band,  $E_v$  is the top edge of the valence band,  $E_F$  is the Fermi level,  $x$  is the Hg<sub>1-x</sub>Cd<sub>x</sub>Te Cd molar composition. The ADP structure consists of an N<sup>+</sup> contact layer (CL), a three-layer multiplication region (ML), an absorber layer (AL), a transition layer (TL), a barrier layer (BL), and a p-n tunneling junction as a top contact layer (CL).

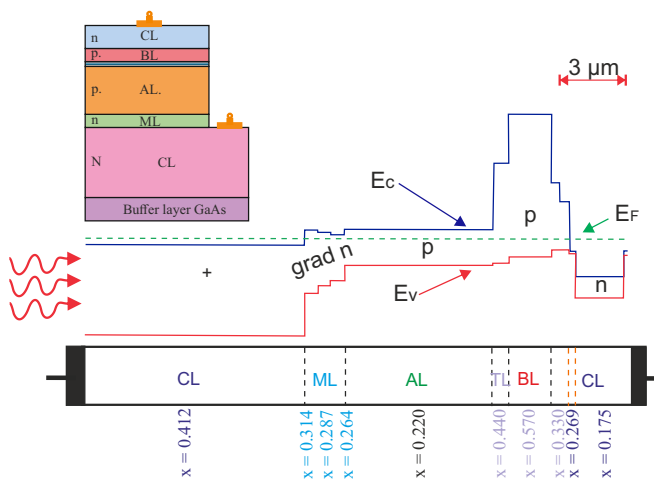


Fig. 1. APD HgCdTe structure with schematic band diagram

The HgCdTe heterostructure was grown in the Aix-200 Aixtron MOCVD system. The HgCdTe growth with the MOCVD technique was described in [5]. Diffusion processes at the growth temperature determine the energy gap profile. In the experiment, the sample has three multiplication layers (ML) with  $x = 0.314$ ,  $0.287$ , and  $0.264$ , respectively, being diffused with very faintly/blurry visible borders. Figure 2 shows the cross-section heterostructure cleavage, taken with an optical (Nomarski) microscope. The total thickness of the HgCdTe device was estimated at  $23.94 \mu\text{m}$ . The thickness of the buffer layer was about  $2.46 \mu\text{m}$ . The three-layer multiplication region cannot be imaged (separated from the absorber layer) due to the process of inter-diffusion during growth [26–29].

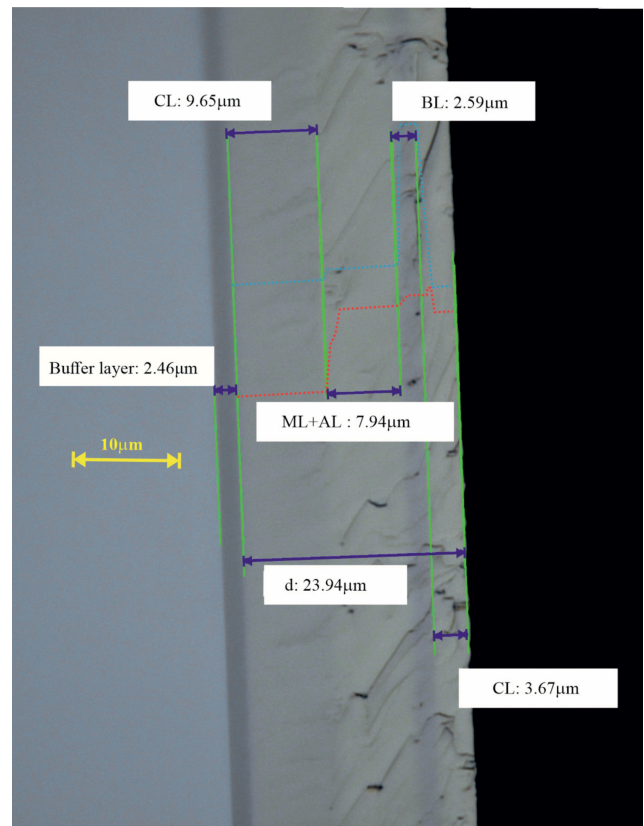
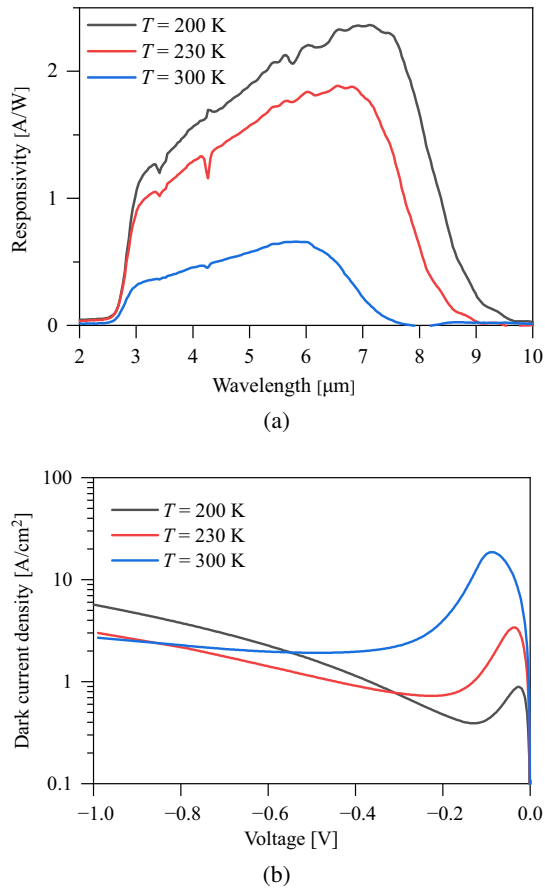


Fig. 2. MOCVD-grown HgCdTe APDs heterostructure on GaAs substrate, taken with an optical microscope

Typical mesa detectors were processed. For further device characterization, spectral response characteristics were studied. Current-voltage ( $J$ - $V$ ) characteristics for selected temperatures were measured by a Keithley 2400 SourceMeter, controlled via the LabView application for automation. Figure 3 shows: (a) the experimental data responsivity versus wavelength (with no bias), and (b) dark current density data versus reverse bias at  $T = 200 \text{ K}$ ,  $T = 230 \text{ K}$ , and  $T = 300 \text{ K}$  for a  $200 \mu\text{m}$  diameter device. The 50% cut-off wavelength is  $\sim 8.2 \mu\text{m}$  at  $200 \text{ K}$  and  $\sim 6.8 \mu\text{m}$  at  $300 \text{ K}$  for the LWIR window. The shift of the LWIR sensitivity edge towards shorter wavelengths indicates that the HgCdTe energy bandgap increases versus temperature. However, in the case of  $J$ - $V$  characteristics, an increase in temperature

## Investigation of HgCdTe avalanche photodiodes for HOT condition



**Fig. 3.** The measured responsivity as a function of wavelength (a) and dark current density versus reverse bias (b) at selected temperatures 200 K, 230 K and 300 K

causes an increase in the dark current and Auger suppression for low voltages of about 0.1 V. For voltages around 1 V, the dark current decreases versus temperature resulting from the increase of HgCdTe energy bandgap contribution to the tunnel current and carrier multiplication. For higher voltages dark current grows faster at lower temperatures. The tunnel current decreases and carrier multiplication is reduced versus bandgap energy. To explain the observed effects, theoretical simulations of the analyzed heterostructures were performed.

### 3. THEORETICAL MODELLING APPROACH

Theoretical modeling was carried out using the commercial program Apsys (Crosslight) [30] to include band-to-band (BTB) tunneling, impact ionization, Auger (1, 7), radiative and Shockley-Read-Hall (SRH) generation-recombination (G-R) mechanisms. Dark current and gain are a set of parameters that always need trade-offs in practical APDs. The proper molar composition and doping gradients were implemented to avoid band discontinuities at the interfaces of individual layers. The cross-section heterostructure cleavage, presented in Fig. 2, showed that the three multiplication layers between the absorber and the  $N^+$  contact layer are invisible. Simulations were carried out for two selected examples: the first one (Profile-1) taking

into account the concentration and Cd composition gradients in three ML layers, and the second (Profile-2) where due to the high composition difference between the  $N^+$  contact and the ML1 layer, one composition and concentration gradient was assumed for the ML1 layer and another for the ML2 and ML3 layers. Figure 4 shows the energy band diagram for both considered cases. For Profile-1, both the valence and conduction bands in the absorber and multiplication areas are smoothed (Fig. 4a), while in the case of Profile-2, the 0.04 eV potential barrier in the conduction band is observed (Fig. 4b). The dominating dark current transport mechanisms mainly depend on the concentration of doping carriers. The SRH and Auger dark currents dominate the dark current at low bias, while BTB tunneling and avalanche components drive  $J$ - $V$  curves at high voltage [31]. An analysis of the influence of diffusion of composition in multiplication layers on the  $J$ - $V$  curves was performed. Figure 5 shows the influence of G-R mechanisms on the dark and photo  $J$ - $V$  characteristics when the structure is polarized in the reverse direction and  $T = 230\text{ K}$ .

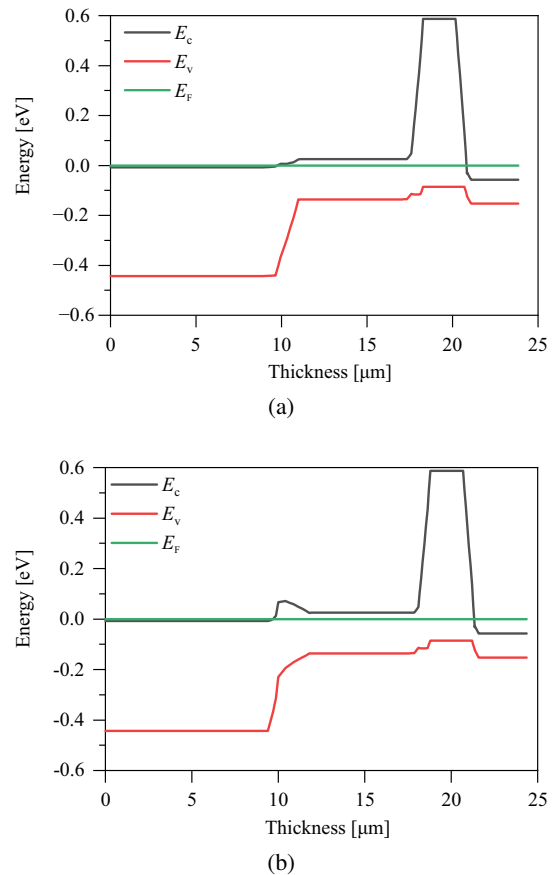


**Fig. 4.** Schematic APD band structure versus thickness at unbiased condition: a) Profile-1; b) Profile-2

The dark current density increases versus voltage while the photocurrent reaches its maximum at  $-0.8\text{ V}$  and then decreases even below the photocurrent resulting only from SRH recombination. The decrease of this photocurrent results from the strong dark current rise. The increase in the dark current caused by the BTB process occurs at reverse voltages above 3.5 V. On the

T. Manyk, J. Sobieski, K. Matuszelański, J. Rutkowski, and P. Martyniuk

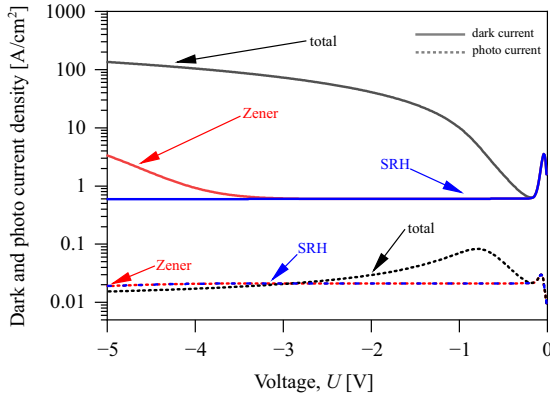


**Fig. 5.** BTB tunneling and impact ionization influence on the dark and photo  $J$ - $V$  characteristic of APD detector

other hand, avalanche multiplication appears at reverse voltages  $>0.3$  V, but clearly depends on the assumed parameters in the Chynoweth model [32].

An analysis of  $a_e$  and the critical field  $b_e$  parameters influence on the carrier multiplication rate were performed and results are presented in Fig. 6.

An increase in both coefficients causes the collision ionization rate to rise, but coefficient  $a_e$  influences the  $J$ - $V$  characteristics

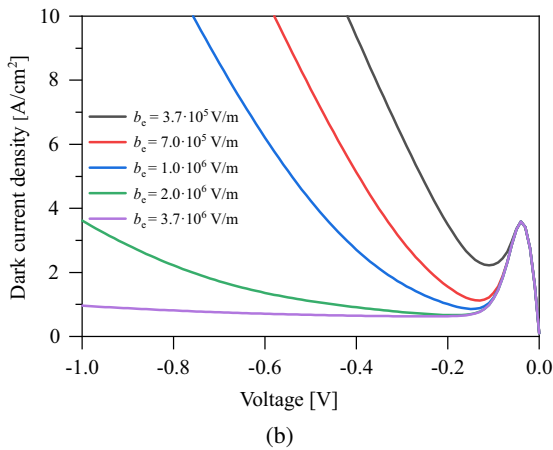
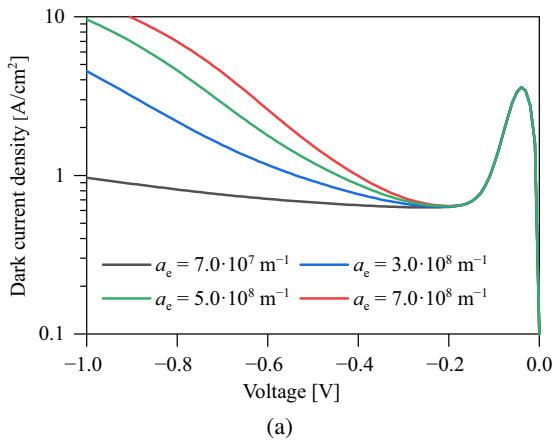


**Fig. 6.** Theoretical simulation of the dark current density dynamics versus reverse bias: a) for selected coefficients  $a_e$  and b) for selected coefficients  $b_e = b_h$

slope (Fig. 6a), while the increase in  $b_e$  coefficient increases the slope and decreases the threshold voltage of the ionization process (Fig. 6b). The proper selection of these parameters makes it possible to match theoretical results to experimental data.

The level of ionization multiplication is also significantly influenced by the level of doping of the absorber. Figure 7 shows the influence of the absorber doping level on the shape of the  $J$ - $V$  characteristics. At low levels of doping, the gain is small and increases versus doping. As doping increases, the rate of Auger recombination also decreases. Reaching the experimentally observed strong suppression of the dark current requires a low carrier concentration in the absorber close to the one assumed in the growth process.

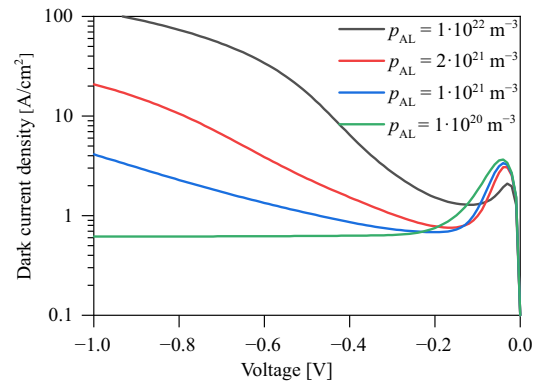


**Fig. 7.** Theoretical simulation of dark current density as a function reverse bias for selected absorber doping levels

The influence of the profile of the multiplication layer on the performance of APDs can already be seen when analyzing the electric field distribution along the profile of the structure.

Figure 8 shows the electric field distribution for Profile-1 (solid line) and Profile-2 (dashed line) in the multiplication layer for two selected voltages  $U = -0.5$  V and  $U = -1.0$  V.

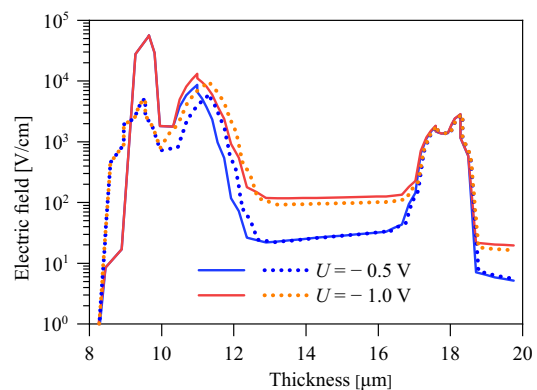


**Fig. 8.** Theoretical simulation of electric field versus the thickness of APDs at  $T = 230$  K for Profile-1 (solid line) and Profile-2 (dashed line) for two polarization voltages  $U = -0.5$  V and  $U = -1.0$  V

Field distributions in the absorber and barrier are comparable in both analyzed cases and an increase in voltage increases the electric field in the absorber. On the other hand, in the multiplication region, in the case of Profile-1, there is a strong increase

## Investigation of HgCdTe avalanche photodiodes for HOT condition

in the electric field independent of polarization, up to 70 kV/cm, which does not affect the multiplication rate. Avalanche multiplication occurs in ML2 and ML3 regions with an electric field of 10 kV/cm. This field increases versus polarization voltage.

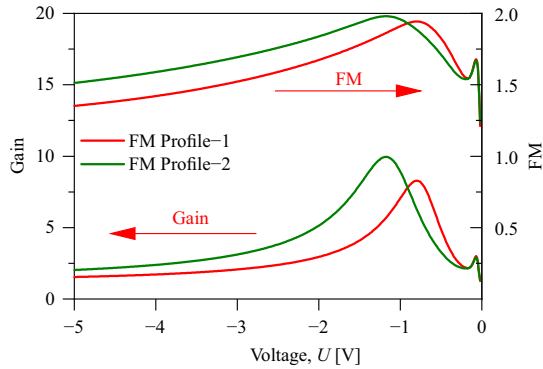


**Fig. 9.** Theoretical simulation data: avalanche gain and the excess noise coefficient (FM) as a function of the reverse bias for the APD structures at the  $T = 230$  K

The multiplication region affects the avalanche gain and the excess noise coefficient (FM) dependence on voltage (Fig. 9). For both cases Profile-1 and Profile-2 we observe two avalanche gain and excess noise maxima, the first small ones related to the Auger suppression, and the second much higher resulting from the impact ionization process (Fig. 9). The first maximum is the same for both multiplication layer designs, while the second is higher for the Profile-2 case and the maximum is shifted towards higher voltage. The decrease of the photocurrent for reverse bias above 1.5 V is caused by suppression of the Auger processes by decreasing the free carrier concentration below its equilibrium values. Figure 10 shows the distribution of electron and hole concentrations for three polarization voltages. We can see that for 0.2 V reverse bias the concentration of electrons drops by three orders of magnitude and the decrease is slower with a further increase in voltage. The avalanche gain, presented in Fig. 9, was calculated as the ratio of photocurrent with the multiplication process to the photocurrent for unbiased conditions.

The excess noise coefficient for LWIR APD for both considered profiles was added to Fig. 9, too. Current gain occurs at

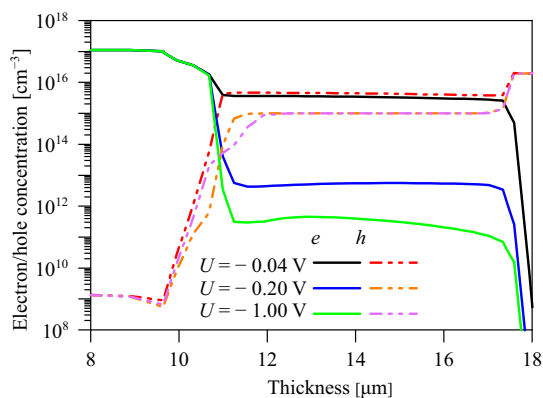
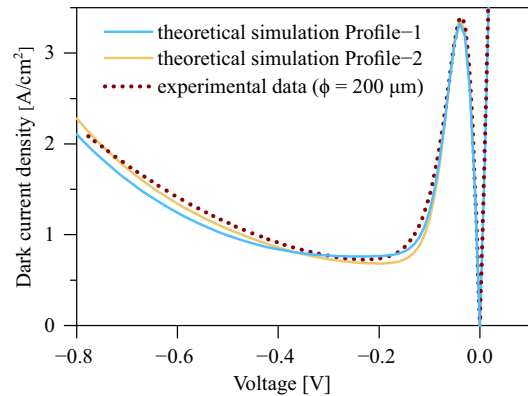


**Fig. 10.** Theoretical modeling of the doping level of electrons and holes as a function of layer thickness for selected bias voltage

low voltage and the reason for its low value is the low acceptor concentration. The decrease in gain versus voltage results from the suppression of the dark current by the Auger mechanism. Small, several-fold gain values were confirmed experimentally.

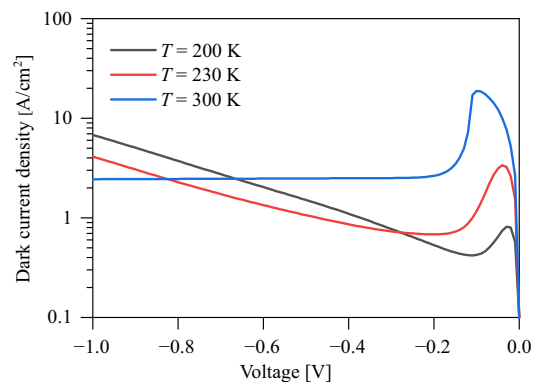
#### 4. THEORETICAL MODELLING APPROACH

Figure 11 shows the theoretical results based on the analysis presented earlier and the experimental characteristics of this detector. We see a fairly good agreement between theory and experience. The  $J$ - $V$  characteristics of the detector at the temperature of 230 K were analyzed in detail reaching the best fit between the theoretical and experimental characteristics for Profile-1 and Profile-2 with the following fitting parameters:  $b_e = b_h = 2.6 \cdot 10^6$  V/m,  $C_n = 3.87 \cdot 10^{-37}$  m<sup>6</sup>s<sup>-1</sup>,  $C_p = 4.45 \cdot 10^{-38}$  m<sup>6</sup>s<sup>-1</sup>,  $\tau_{srh-e} = 100$  ns,  $\tau_{srh-h} = 10$  ns. Theoretical simulation and fit to the measured results for Profil-1 was reached assuming coefficients  $a_e = 8.8 \cdot 10^7$  m<sup>-1</sup>,  $a_h = 8.8 \cdot 10^5$  m<sup>-1</sup> and for Profil-2  $a_e = 6.9 \cdot 10^7$  m<sup>-1</sup>,  $a_h = 6.9 \cdot 10^5$  m<sup>-1</sup>.



**Fig. 11.** Theoretical (Profile-1 and Profile-2) and experimental data dark current density as a function of the reverse bias at 230 K

Theoretical analysis of the  $J$ - $V$  as a function of temperature was also performed. The theoretical simulated data obtained for Profile-2 is presented in Fig. 12. Comparing the experimental data (see Fig. 3b) and theoretical modeling data (see Fig. 12), a proper agreement between theory and experiment can be seen.



**Fig. 12.** Theoretical dark current density data as a function reverse bias at 200 K, 230 K, and 300 K

## 5. CONCLUSIONS

The performance of LWIR HgCdTe APDs at HOT conditions was presented. The band diagram of HgCdTe heterostructure grown on GaAs substrate by MOCVD was investigated. Theoretical simulations were performed for APDs optimized for 8  $\mu\text{m}$  at 230 K. The influence of both BTB and impact ionization on the  $J$ - $V$  characteristics was studied. The Zener mechanism influences the diode performance  $> 4$  V, while the impact ionization mechanism drives the performance for  $> 0.2$  V. The theoretical simulation indicates that the geometry, carrier concentration within the absorber, and the multiplication layer control the impact ionization process. The proper agreement between the theoretical simulation and the experimental data allowed us to determine the parameters of the investigated heterostructure.

## ACKNOWLEDGEMENTS

This work was supported by the National Science Centre (Poland), grants No. OPUS-2019/33/B/ST7/00614.

## REFERENCES

- [1] A. Rogalski, "HgCdTe infrared detector material: history, status and outlook," *Rep. Prog. Phys.*, vol. 68, no. 10, pp. 2267–2336, Oct. 2005, doi: [10.1088/0034-4885/68/10/R01](https://doi.org/10.1088/0034-4885/68/10/R01).
- [2] M.A. Kinch, *Fundamentals of infrared detector materials*. in Tutorial texts series, no. v. TT76. Bellingham, Wash: SPIE Press, 2007.
- [3] W. Hu *et al.*, "128 $\times$ 128 long-wavelength/mid-wavelength two-color HgCdTe infrared focal plane array detector with ultralow spectral cross talk," *Opt. Lett.*, vol. 39, no. 17, p. 5184, Sep. 2014, doi: [10.1364/OL.39.005184](https://doi.org/10.1364/OL.39.005184).
- [4] K. Jóźwikowski, M. Kopytko, A. Rogalski, and A. Jóźwikowska, "Enhanced numerical analysis of current-voltage characteristics of long wavelength infrared n-on-p HgCdTe photodiodes," *J. Appl. Phys.*, vol. 108, no. 7, p. 074519, Oct. 2010, doi: [10.1063/1.3483926](https://doi.org/10.1063/1.3483926).
- [5] W. Gawron, J. Sobieski, T. Manyk, M. Kopytko, P. Madejczyk, and J. Rutkowski, "MOCVD Grown HgCdTe Heterostructures for Medium Wave Infrared Detectors," *Coatings*, vol. 11, no. 5, p. 611, May 2021, doi: [10.3390/coatings11050611](https://doi.org/10.3390/coatings11050611).
- [6] A. Rogalski, *Infrared and Terahertz Detectors, Third Edition*. CRC Press, 2019. doi: [10.1201/b21951](https://doi.org/10.1201/b21951).
- [7] X. Li *et al.*, "Controlling of Avalanche Dark Carriers in Realizing Hot Single Photon Detector," *IEEE Electron Device Lett.*, vol. 43, no. 6, pp. 922–925, Jun. 2022, doi: [10.1109/LED.2022.3167765](https://doi.org/10.1109/LED.2022.3167765).
- [8] A.K. Storebø, T. Brudevoll, E. Selvig, R.W. Hansen, T. Lorenzen, and R. Haakenaasen, "Effect of the Series Resistance on the Current Response of a HgCdTe Avalanche Photodiode Under High-intensity Nanosecond Irradiation," *J. Electron. Mater.*, vol. 51, no. 7, pp. 4029–4039, Jul. 2022, doi: [10.1007/s11664-022-09670-z](https://doi.org/10.1007/s11664-022-09670-z).
- [9] J. Rothman *et al.*, "HgCdTe APDs detector developments for high speed, low photon number and large dynamic range photodetection," in *International Conference on Space Optics – ICSO 2020*, Z. Sodnik, B. Cugny, and N. Karafolas, Eds., Online Only, France: SPIE, Jun. 2021, p. 15. doi: [10.1117/12.2599159](https://doi.org/10.1117/12.2599159).
- [10] L. Yang *et al.*, "Modeling and characteristics of MWIR HgCdTe APD at different post-annealing processes," *Infrared Phys. Technol.*, vol. 127, p. 104413, Dec. 2022, doi: [10.1016/j.infrared.2022.104413](https://doi.org/10.1016/j.infrared.2022.104413).
- [11] H. Guo *et al.*, "Developments and characterization of HgCdTe e-APDs at SITP," in *Earth and Space: From Infrared to Terahertz (ESIT 2022)*, J. Chu, Ed., Nantong, China: SPIE, Jan. 2023, p. 72. doi: [10.1117/12.2665280](https://doi.org/10.1117/12.2665280).
- [12] X. Han *et al.*, "Dark current and noise analysis for Long-wavelength infrared HgCdTe avalanche photodiodes," *Infrared Phys. Technol.*, vol. 123, p. 104108, Jun. 2022, doi: [10.1016/j.infrared.2022.104108](https://doi.org/10.1016/j.infrared.2022.104108).
- [13] J. Rothman, L. Mollard, S. Gout, L. Bonnefond, and J. Wlasow "History-Dependent Impact Ionization Theory Applied to HgCdTe e-APDs," *J. Electron. Mater.*, vol. 40, no. 8, pp. 1757–1768, 2011, doi: [10.1007/s11664-011-1679-9](https://doi.org/10.1007/s11664-011-1679-9).
- [14] R. Xie *et al.*, "Spatial description theory of narrow-band single-carrier avalanche photodetectors," *Opt. Express*, vol. 29, no. 11 pp. 16432–16446, 2021, doi: [10.1364/OE.418110](https://doi.org/10.1364/OE.418110).
- [15] S. Selberherr, *Analysis and simulation of semiconductor devices*. Wien, Austria; New York: Springer-Verlag, 1984.
- [16] A.G. Chynoweth, "Ionization Rates for Electrons and Holes in Silicon," *Phys. Rev.*, vol. 109, no. 5, pp. 1537–1540, Mar. 1958, doi: [10.1103/PhysRev.109.1537](https://doi.org/10.1103/PhysRev.109.1537).
- [17] J.D. Beck, C.-F. Wan, M.A. Kinch, and J.E. Robinson, "MWIR HgCdTe avalanche photodiodes," *International Symposium on Optical Science and Technology*, R.E. Longshore, Ed., USA, Nov. 2001, p. 188, doi: [10.1117/12.448174](https://doi.org/10.1117/12.448174).
- [18] M.B. Reine *et al.*, "HgCdTe MWIR back-illuminated electron-initiated avalanche photodiode arrays," *SPIE Optics + Photonics*, R.E. Longshore and A. Sood, Eds., USA, Aug. 2006, p. 629403, doi: [10.1117/12.692872](https://doi.org/10.1117/12.692872).
- [19] A. Singh, V. Srivastav, and R. Pal, "HgCdTe avalanche photodiodes: A review," *Opt. Laser Technol.*, vol. 43, no. 7, pp. 1358–1370, Oct. 2011, doi: [10.1016/j.optlastec.2011.03.009](https://doi.org/10.1016/j.optlastec.2011.03.009).
- [20] Y. Cheng, L. Chen, H. Guo, C. Lin, and L. He, "Improved local field model for HgCdTe electron avalanche photodiode," *Infrared Phys. Technol.*, vol. 101, pp. 156–161, Sep. 2019, doi: [10.1016/j.infrared.2019.07.002](https://doi.org/10.1016/j.infrared.2019.07.002).
- [21] M. Kopytko, J. Sobieski, R. Xie, K. Jóźwikowski, and P. Martyniuk, "Impact ionization in HgCdTe avalanche photodiode optimized to 8  $\mu\text{m}$  cut-off wavelength at 230 K," *Infrared Phys. Technol.*, vol. 115, p. 103704, Jun. 2021, doi: [10.1016/j.infrared.2021.103704](https://doi.org/10.1016/j.infrared.2021.103704).
- [22] J. Beck *et al.*, "The HgCdTe electron avalanche photodiode," *J. Electron. Mater.*, vol. 35, no. 6, pp. 1166–1173, Jun. 2006, doi: [10.1007/s11664-006-0237-3](https://doi.org/10.1007/s11664-006-0237-3).
- [23] M.A. Kinch, J.D. Beck, C.-F. Wan, F. Ma, and J. Campbell, "HgCdTe electron avalanche photodiodes," *J. Electron. Mater.*, vol. 33, no. 6, pp. 630–639, Jun. 2004, doi: [10.1007/s11664-004-0058-1](https://doi.org/10.1007/s11664-004-0058-1).
- [24] A. Singh, A.K. Shukla, and R. Pal, "HgCdTe e-avalanche photodiode detector arrays," *AIP Adv.*, vol. 5, no. 8, p. 087172, Aug. 2015, doi: [10.1063/1.4929773](https://doi.org/10.1063/1.4929773).
- [25] J. He *et al.*, "Design of a bandgap-engineered barrier-blocking HOT HgCdTe long-wavelength infrared avalanche photodiode," *Opt. Express*, vol. 28, no. 22, p. 33556, Oct. 2020, doi: [10.1364/OE.408526](https://doi.org/10.1364/OE.408526).
- [26] X. Wang *et al.*, "Study of gain and photoresponse characteristics for back-illuminated separate absorption and multiplication GaN avalanche photodiodes," *J. Appl. Phys.*, vol. 115, no. 1, p. 013103, Jan. 2014, doi: [10.1063/1.4861148](https://doi.org/10.1063/1.4861148).

## Investigation of HgCdTe avalanche photodiodes for HOT condition

- [27] T. Manyk, K. Majkowycz, J. Rutkowski, and P. Martyniuk, “Theoretical study of back-to-back avalanche photodiodes for dual-band infrared applications,” *Opto-Electron. Rev.*, vol. 31, no. 2, p. e145093, Aug. 2023, doi: [10.24425/opelre.2023.145093](https://doi.org/10.24425/opelre.2023.145093).
- [28] T.J. de Lyon *et al.*, “MBE growth of HgCdTe avalanche photodiode structures for low-noise 1.55  $\mu\text{m}$  photodetection,” *J. Cryst. Growth*, vol. 201–202, pp. 980–984, May 1999, doi: [10.1016/S0022-0248\(98\)01506-1](https://doi.org/10.1016/S0022-0248(98)01506-1).
- [29] D. Chen *et al.*, “Photon-trapping-enhanced avalanche photodiodes for mid-infrared applications,” *Nat. Photon.*, vol. 17, no. 7, pp. 594–600, Jul. 2023, doi: [10.1038/s41566-023-01208-x](https://doi.org/10.1038/s41566-023-01208-x).
- [30] Crosslight Software Inc. *Crosslight Device Simulation Software – General Manual 2019 version*. 2019, p. 1369. [Online] Available: <https://crosslight.com/>
- [31] J. Chen *et al.*, “High-performance HgCdTe avalanche photodiode enabled with suppression of band-to-band tunneling effect in mid-wavelength infrared,” *Quantum Mater.*, vol. 6, no. 1, p. 103, Dec. 2021, doi: [10.1038/s41535-021-00409-3](https://doi.org/10.1038/s41535-021-00409-3).
- [32] G. Leveque, M. Nasser, D. Bertho, B. Orsal, and R. Alabedra, “Ionization energies in  $\text{Cd}_x\text{Hg}_{1-x}\text{Te}$  avalanche photodiodes,” *Semicond. Sci. Technol.*, vol. 8, no. 7, pp. 1317–1323, Jul. 1993, doi: [10.1088/0268-1242/8/7/021](https://doi.org/10.1088/0268-1242/8/7/021).